Practical method for the design of pretensioned fully grouted rockbolts in tunnels

PAPER • OPEN ACCESS

The operational space for divertor power exhaust in DEMO with a super-X divertor

IOP Publishing | International Atomic Energy Agency Nuclear Fusion

Nucl. Fusion **61** (2021) 076007 (14pp) https://doi.org/10.1088/1741-4326/abf9df

The operational space for divertor power exhaust in DEMO with a super-X divertor

L. Xiang[1,*], F. Militello[1], D. Moulton[1], F. Subba[2], L. Aho-Mantila[3], D. Coster[4], M. Wensing[5], T. Lunt[4], M. Wischmeier[4] and H. Reimerdes[5]

[1] Culham Centre for Fusion Energy, UKAEA, Abingdon, OX14 3DB, United Kingdom
[2] Politecnico di Torino, Corso Duca degli Abruzzi 24, 10129, Torino, Italy
[3] Technical Research Centre of Finland, FI-02044 VTT, Finland
[4] Max-Planck Institut für Plasmaphysik, D-85748 Garching, Germany
[5] Ecole Polytechnique Fédérale de Lausanne (EPFL), Swiss Plasma Center (SPC), CH-1015 Lausanne, Switzerland

E-mail: lingyan.xiang@ukaea.uk

Received 29 January 2021, revised 14 April 2021
Accepted for publication 20 April 2021
Published 31 May 2021

Abstract

SOLPS-ITER simulations of the European DEMO reactor with a Super-X divertor, which has larger major radius at the outer target and increased connection length, show an increased operational space for divertor power exhaust compared to the conventional single-null configuration. Using a multi-fluid approach with fluid neutrals and charge-state bundling of impurities, we assessed the existence and boundaries of the operational space in the single-null and Super-X configurations by carrying out fuelling, seeding and power scans. Compared to the conventional single-null divertor, the Super-X divertor offers lower impurity concentration (factor ∼2 lower) at the same main plasma density, and consistent with this, it has lower main plasma density at the same impurity concentration level. This observed difference is in line with the simple analytical Lengyel model predictions resulting from the increased connection length in the super-X configuration. DEMO with a Super-X divertor demonstrates remarkable robustness against increases in input power, and in this study is able to exhaust the maximum expected steady-state separatrix-crossing power of 300 MW while maintaining acceptable impurity concentration along the separatrix This is something that was not possible in the single-null configuration in this study. This robustness of the Super-X divertor lies mostly in its capability to sufficiently dissipate power in its divertor via argon (Ar) radiation at acceptable Ar concentration, which is related to two factors: long (with respect to single-null) parallel connection length from the upstream to the outer target and higher but tolerable extrinsic impurity concentration at higher input powers. Finally, consistent with neon-seeded simulations of ITER, it is observed in all our simulations that the plasma density drops with increasing Ar concentration given fixed power input. We find that as the Ar content increases, the accompanying enhancement of Ar radiation reduces the power available for deuterium (D) to be ionized, thus limiting the D ionization particle source, and consequently reducing the plasma density.

*Author to whom any correspondence should be addressed.

Keywords: radiative power dissipation, super-X divertor configuration, multi-fluid modelling, Lengyel model, operational space (for divertor power exhaust)

(Some figures may appear in colour only in the online journal)

1. Introduction

The European fusion reactor DEMO is designed to produce 2 GW of fusion power [1]. Of this power, 20% goes to α-particles that heat the plasma and needs ultimately to be handled in some way. In addition, the auxiliary heating schemes mainly for plasma control purposes will lend another 50 MW [2, 3] to the hot plasma. The total power to be exhausted thus tallies to 450 MW. In the current design, 2/3 of this power is to be dissipated within the confined region of the plasma, of which about 150 MW is in the form of bremsstrahlung and synchrotron radiation by charged particles [4] and another 150 MW is via impurity line radiation. The power left to cross the separatrix into the plasma boundary region, denoted as $P_{\rm SOL}$, is about 150 MW, which is just above the L–H transition threshold. The average power load to the divertor targets, assuming no power lost to the main chamber wall (mcw) via cross-field transport or power loss due to A & M processes and radiation, i.e. *unmitigated* power load, can be estimated as:

$$q_{\perp,\rm t} = q_{\parallel,\rm t} \times \sin\,\alpha = \frac{f_{\rm odiv} \times P_{\rm SOL}}{2\pi R_{\rm t} \times \lambda_q \times \sin\,\theta}\frac{1}{R_{\rm t}/R_{\rm u}} \times \sin\,\alpha, \qquad (1)$$

where $f_{\rm odiv}$ is the fraction of $P_{\rm SOL}$ that goes to the outer divertor, α is the field line incident angle at the divertor target, θ is the upstream magnetic field pitch angle and $R_{\rm t}, R_{\rm u}$ are the major radius at the outer divertor target and outboard midplane (OMP). The 'u' and 't' in the subscript will be used to denote '*upstream*' and '*target*' throughout the paper. $R_{\rm u} = R_0 + a$, with R_0 being the major radius at the magnetic axis and a being the plasma minor radius. λ_q is the power decay length at the OMP.

Substituting the design parameters of DEMO conventional single-null (SN) divertor configuration [5], namely $P_{\rm SOL} = 150$ MW, $R_0 = 8.9$ m, $a = 2.87$ m, $\lambda_q = 3$ mm, $\theta = 20^\circ$, $R_{\rm t}/R_{\rm u} = 0.71$, $\alpha = 1.5^\circ$ and assuming $f_{\rm odiv} = 50\%$, into equation (1), we have $q^{\rm SN}_{\perp,\rm t} \approx 36$ MW m^{-2}. Note that $\alpha = 1.5^\circ$ is a rather optimistic assumption here. The other parameters of DEMO include elongation, $\kappa_{95} = 1.65$, plasma current, $I_P = 19.1$ MA, axis magnetic field, $B_0 = 4.9$ T and poloidal magnetic field at the OMP, $B_{\rm Pu} = 1.3$ T. The current engineering limit of the stationary power load on the tungsten divertor plate for sufficient duty cycle is about 10 MW m^{-2} [6]. Taking into consideration the degradation of material properties due to neutron irradiation, and the power load due to photons and surface recombination onto the material surface, the tolerated *plasma heat flux* onto the divertor plates is about $q^{\rm limit}_{\perp,\rm t} = 5$ MW m^{-2} [7, 8]. This limiting value is factor $\sim$7 lower than the estimated unmitigated power flux, which means that the excessive 86% of the power therefore needs to be radiated away mainly by extrinsic impurities in the narrow plasma boundary region.

High impurity concentration in the vicinity of the main plasma threatens to compromise the fusion performance if the impurities get transported further inside the confined region. Some alternative divertor configuration designs guided by theory could be able to ease the burden of power exhaust in the plasma boundary region. In this work, effort has been made to assess if the Super-X divertor (SXD) configuration harbours safe divertor operation without accumulating high impurity concentration near the confined region. We will present the most recent results of the study on the SXD configuration for DEMO [5] in the following. The extrinsic impurity investigated is argon (Ar), with its concentration defined as $c_{\rm Ar} = n_{\rm Ar}/n_{\rm e}$, where $n_{\rm Ar}$ is the Ar ion density. New results of other alternative configurations, such as double-null and X-divertor are reported in [9, 10].

2. DEMO divertor configurations

2.1. Super-X divertor (SXD) and single-null divertor (SND) configurations for DEMO

A poloidal cross-sectional view of the DEMO SXD configuration is given in figure 1, on top of the DEMO SND configuration. The targets have been slightly modified to enforce 1.5° of field line incident angle across 3 mm distance on either side of the separatrix in both configurations. Due to the limit on TF coils stress and the requirement of remote handling, the outer target of the SXD is set to a similar major radius as the OMP, whose position is marked out in the figure. The toroidal flux expansion, $f_x = R_{\rm t}/R_{\rm u}$, is $f_x = 0.92$. Substituting the design parameters of DEMO SXD into equation (1), one sees that DEMO SXD, with factor $\sim$1.33 higher toroidal flux expansion than SND, has an *unmitigated* power flux to the target of $q^{\rm SX}_{\perp,\rm t} \approx 26$ MW m^{-2} at $P_{\rm SOL} = 150$ MW. Now, about 80% of $P_{\rm SOL}$ needs to be radiated in the plasma boundary and divertor volume. The longer connection length to the outer target in the SXD offers further advantages over the conventional SND.

The SXD has longer parallel connection lengths from the OMP to the outer divertor target, $L_{\parallel,\rm ot}$, than the conventional SND. The ratio $L^{\rm SX}_{\parallel,\rm ot}/L^{\rm SN}_{\parallel,\rm ot}$ is $\geqslant 1.75$ in the radial range of 3 mm mapped to the OMP, i.e. the aimed value of λ_q, as given in table 1. The two-point model predicts $T_{\rm u}^{7/2} - T_{\rm t}^{7/2} = \frac{7}{2}\frac{q_{\parallel,\rm u}}{\kappa_{\rm e0,\parallel}} \times L_\parallel$ [11], according to which longer connection length means lower divertor target temperature in the absence of radiation in the divertor, given comparable upstream plasma conditions. Furthermore, the parallel connection lengths from the OMP to the inner and outer divertor targets, $L_{\parallel,\rm it}, L_{\parallel,\rm ot}$, are rather

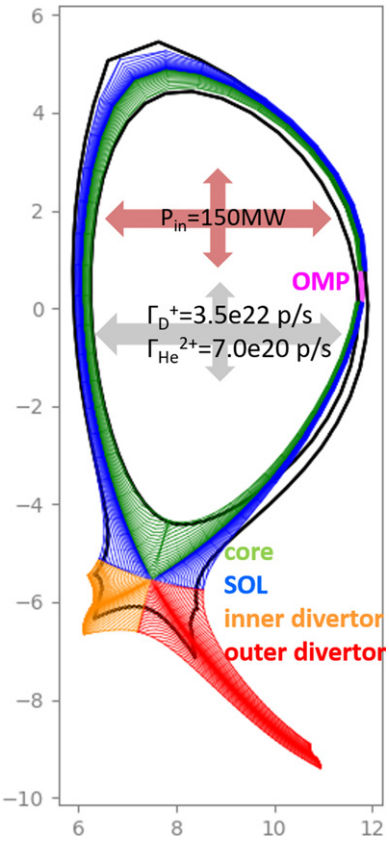

Figure 1. Poloidal cross-section of the DEMO SXD configuration used in SOLPS-ITER simulation, on top of the outline of the poloidal cross-section of the DEMO SND configuration in black. coloured regions form the modelling domain, and they are: the 'core' (*magenta*), SOL (*blue*), inner divertor (*orange*), denoted as *idiv* and outer divertor (*red*), denoted as *odiv* henceforth in the figures. This notation of regions will be used in the following sections when modelling results are discussed. Location of the OMP is marked in magenta.

comparable in the DEMO SXD. Their ratio $L_{\parallel,\mathrm{it}}/L_{\parallel,\mathrm{ot}}$ is in the range of 1.08–1.3 in the radial range of 3 mm, compared to 1.3–1.95 in the DEMO SND. According to the two-point model, this may contribute to better symmetry between the inner and outer divertor in the SXD [12], as the model predicts that $q_{\parallel,\mathrm{odiv}}/q_{\parallel,\mathrm{idiv}} \propto L_{\parallel,\mathrm{it}}/L_{\parallel,\mathrm{ot}}$, where '*odiv*' and '*idiv*' stand for outer divertor and inner divertor. At the radial location of 3 mm, the connection length to the inner and outer divertor targets is given in table 1. The values of the SND are also provided as reference.

2.2. Simulation setup

More realistic estimation of the target power load in the DEMO SXD needs to be done through comprehensive study with models more complete than the 0D two-point model. The code package SOLPS-ITER [13, 14], which consists mainly of 2D fluid plasma code B2.5 [15] and 3D kinetic neutral code EIRENE [16, 17], is implemented with vigorous boundary plasma physics models. The aim of this study is to assess the accessibility of the *operational space* of the DEMO SXD and how it compares to that of the DEMO SND configuration. The constraints used to define the operational space for DEMO reflect the considerations of ensuring sufficient lifetime of the divertor targets and simultaneously safeguarding fusion performance in the confined region.

We use the SOLPS-ITER code with fluid neutrals and Ar charge-state bundling in order to shorten the computational time to accommodate large parameter scans. In dense and cold divertor plasma conditions, the plasma and neutral densities are expected to be high and fluid neutral temperature (same as ions) low. The mean free path of neutrals is short with respect to the DEMO divertor size. The SXD has width $\geqslant$50 cm and length $\approx$5 m, and the SND's width is $\geqslant$1 m and length is $\approx$2 m, see figures 1 and 2 in [5], as well as figure 1 above. After mathematical estimation of the neutrals' (D^0 and Ar^0) mean free path in the simulations with cold divertor condition ($T_{\mathrm{e,target}} \leqslant 5$ eV and $n_{\mathrm{e,target}} \geqslant 5 \times 10^{20}$ m^{-3}) is in the order of cm. Therefore, the fluid neutrals' approach is considered appropriate here. Note that with a fluid neutral model, we do not treat deuterium (D) molecules. We consider a D plasma, with intrinsic impurity helium (He) and extrinsic impurity Ar. Ar is bundled into effectively three charge states: Ar^0, $Ar^{1^+-17^+}$, Ar^{18^+}. The rate coefficients of the effective charge state $Ar^{1^+-17^+}$ are computed from the ADAS rate coefficients of unbundled Ar using a charge-state weighing algorithm introduced in [18, 19]. Due to the method of charge-state bundling, any enhancement of the electron cooling coefficient function due to impurity transport is not accounted for [20]. All the neutral atoms are considered as fluids, as are all the charged species. The particle diffusivity is $D_\perp = 0.1$ m^2 s^{-1}. The thermal conductivity of electrons and ions is $\chi_{\perp,\mathrm{e,i}} = 0.1$ m^2 s^{-1} from -10 mm to -2.5 mm inside the separatrix, which increases to 0.3 m^2 s^{-1} at the separatrix, and remains at 0.3 m^2 s^{-1} in the SOL. Both $D_\perp$ and $\chi_{\perp,\mathrm{e,i}}$ are down-scaled from the values used in ITER SOLPS-ITER simulations to obtain a power decay length at the OMP of $\lambda_q = 3$ mm. To assess the operational space, we varied both the D fuelling and Ar seeding rates, thus scanning an array of combinations of these two parameters. The ranges covered in the scan are: $\Gamma_{\mathrm{D^0}} = 2.55 \times 10^{22} \rightarrow 2.55 \times 10^{24}$ and $\Gamma_{\mathrm{Ar^0}} = 3.5 \times 10^{19} \rightarrow 3.5 \times 10^{21}$, with the unit particle/s (p s^{-1}). In the fluid neutral model, the D and Ar puff is done in such a simplified manner for it to be introduced homogeneously from the entire SOL boundary. During the scan, we obtained a wide range of divertor conditions. We did the scan in the same manner for the SND, which covered very similar ranges of fuelling and seeding as the SXD. At the core boundary, i.e. the innermost green contour in figure 1, we imposed a D ion flux of $\Gamma_{\mathrm{D^+}} = 3.5 \times 10^{22}$ p s^{-1} to account for pellet fuelling, a He ion flux of $\Gamma_{\mathrm{He^{2+}}} = 7.0 \times 10^{20}$ p s^{-1} to be the slowed-down α-particle during the 2 GW fusion reaction and input power P_{in} of 150 MW split evenly into electron and ion channels entering the simulation domain.[6] To test the robustness of the DEMO

[6] P_{in} is similar to the aforementioned P_{SOL} in the context of SOLPS-ITER modelling. Strictly speaking, they are not the same, as P_{in} refers the power into the simulation domain at the core boundary. But since the part of the simulation domain inside the separatrix is thin compared to the entire confined region, as can be seen in figure 1. P_{in} and P_{SOL} are *effectively* equivalent, and mostly P_{in} will be used when talking about SOLPS-ITER simulations.

Table 1. $L_{\parallel,\mathrm{it}}$, $L_{\parallel,\mathrm{ot}}$ are the parallel connection lengths from the OMP to the inner targets and outer target, respectively. α is the field line incident angle at the target in the width of the power decay length (in our study it is aimed at 3 mm) λ_q on both sides of the strike point. f_x is the toroidal flux expansion at the outer target. Values are given here for the flux tube at 3 mm distance from the separatrix in the scrape-off layer (SOL).

Parameters	SXD	SND
$L_{\parallel,\mathrm{it}}$	226 m	191 m
$L_{\parallel,\mathrm{ot}}$	175 m	100 m
$L_{\parallel,\mathrm{it}}/L_{\parallel,\mathrm{ot}}$	1.30	1.91
α	$\approx 1.5^\circ$	$\approx 1.5^\circ$
f_x	≈ 1	≈ 0.75

SX divertor against P_{SOL} fluctuations, we also performed simulations at an increased power input of 300 MW, assuming the extreme case where no line radiation happens in the core region.

3. Operational space for DEMO divertor power exhaust

A DEMO plasma must satisfy *at the least* the following three requirements concerning the plasma side to be considered as operationally viable: (1) no disruptions or H–L back transition due to too high plasma density, (2) long enough lifetime of the divertor plasma facing components (PFCs) and (3) low impurity level in the main plasma to safeguard sufficiently high rate of fusion reaction in the core. These requirements are quantified as constraints imposed on certain plasma parameters in this work to easily assess if they are satisfied by a simulated DEMO plasma. The constraints are the following:

- The stationary peak plasma power flux at all targets is below the limit for tungsten, i.e. $q_{\perp,\mathrm{t}} \leqslant 5$ MW m^{-2}.
- The target temperature is sufficiently low to avoid significant tungsten net erosion. We set the limit to be $T_{\mathrm{t}} \leqslant 5$ eV.
- The density at the separatrix, $n_{\mathrm{e,sep}}$, does not exceed some fraction of the Greenwald density limit n_{GW} to sail safely below the density limit disruption and avoid H–L back transition at high densities. For DEMO, $n_{\mathrm{GW}} = 7.3 \times 10^{19}$ m^{-3}. We put a constraint of $n_{\mathrm{e,sep}} \leqslant 0.6 n_{\mathrm{GW}} \approx 4.4 \times 10^{19}$ m^{-3}.
- The extrinsic impurity concentration in the immediate vicinity of the confined region should not be too high to spoil the fusion performance. SOLPS-ITER may not model the impurity transport in the confined region well. We nevertheless limit the Ar concentration at the separatrix of the confined region to be $c_{\mathrm{Ar,sep}} \leqslant 1\%$, but rather trust the comparison between configurations and power levels.

A modelled plasma, which simultaneously meets these constraints, is considered to be within the *operational space*.

3.1. Operational space in DEMO SXD and SND at two power levels

Applying these constraints to the simulations with a fuelling and seeding rates scan, we identify whether an operational space exits for a given divertor configuration and power level, and if this is the case, what the differences are in parameters of interest between the different configurations and input powers inside the operational space.

An operational space *could* be found for both the SND and SXD when we impose 150 MW crossing the core boundary. But only the SXD has operational space at $P_{\mathrm{in}} = 300$ MW, while *no* acceptable solution could be found for the SND at this input power. In section 1, it is shown that in the DEMO SND with $P_{\mathrm{in}} = 150$ MW the plasma boundary region needs to dissipate about 86% of P_{SOL} to reduce the target power flux from the *unmitigated* value of 36 MW m^{-2} to the safe value of 5 MW m^{-2}. Present-day tokamaks have reported a main plasma radiation fraction of 50%–70% and the radiation fraction in the plasma boundary to be even lower [21–24]. The existence of the operational space for the SXD and particularly SND at $P_{\mathrm{in}} = 150$ MW is thus encouraging. The plasma conditions at the separatrix concern both the core performance and divertor conditions. A good way to display our results is to plot the separatrix Ar concentration as a function of the separatrix density, the former representing the amount of impurities needed to dissipate the plasma power and the amount of dilution, the latter measuring core performance (lower density leads to improved pedestals). We plot these quantities for our database in figure 2.

Shown in this figure is the Ar concentration averaged along the separatrix above the X-point, $\bar{c}_{\mathrm{Ar,sep}}$, and the density at the OMP, $n_{\mathrm{e,sep}}$ for all simulations of the DEMO SND with $P_{\mathrm{in}} = 150$ MW and the DEMO SXD with P_{in} being 150 and 300 MW. The SND with $P_{\mathrm{in}} = 300$ MW does not have an operational space found in the simulations, hence its data point is not shown in this figure. One can see that the data points of a configuration or an input power level collapse onto a distinctive curve. One can also see that all the curves can be fitted with roughly a dependency of $\bar{c}_{\mathrm{Ar,sep}} \propto n_{\mathrm{e}}^{-4}$. The figure reveals that:

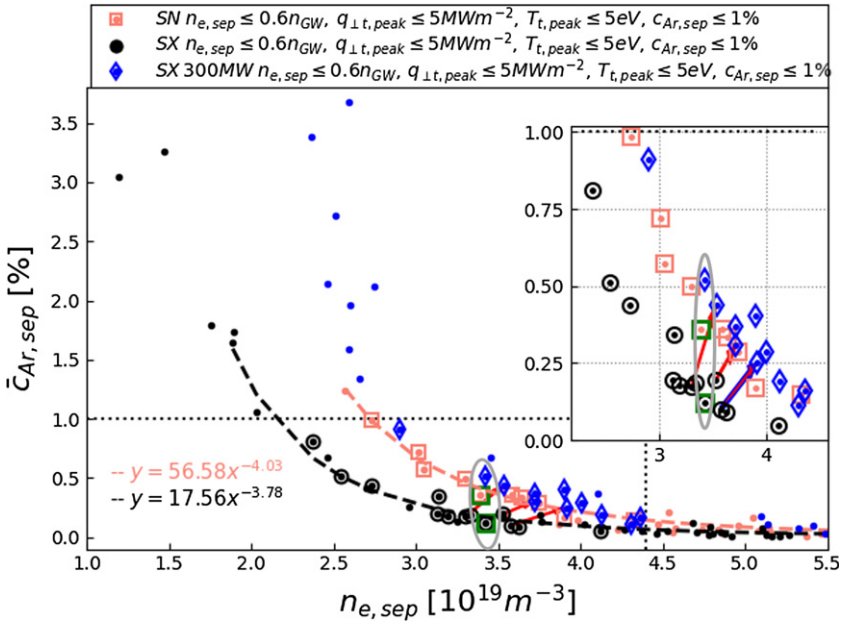

Figure 2. Average Ar concentration along the separatrix $\bar{c}_{\mathrm{Ar,sep}}$ as a function of the density at the OMP separatrix $n_{\mathrm{e,sep}}$ for all the simulations done for a configuration (SX or SN) or an input power level ($P_{\mathrm{in}} = 150$ MW or 300 MW). Among them, the simulations whose plasma is within the operation space are also marked with symbols (square, circle, diamond). Black and pink dash lines are the power-law fit to the data points of SX and SN, both showing a roughly $\bar{c}_{\mathrm{Ar,sep}} \propto n_{\mathrm{e}}^{-4}$ dependency. Inset shows only the points within the operation space. Three red arrows mark three pairs of simulations of the SXD with the same fuelling and seeding rates with only P_{in} being different. Pair marked by the red arrow with blue outline (rightmost) is compared in figures 7 and 8. Two green square symbols (also shown in the inset) mark the two simulations, one SND and one SXD, to be compared in figure 3(*b*) and figure 4. The three simulations outlined by the grey ellipse are to be compared in figure 6.

(a) At the same density (*Ar concentration*), the DEMO SXD has lower Ar concentration (*density*) than the SND. The inset in the figure, showing the operational points only, demonstrates that the difference is nearly a factor of 2. Furthermore, within the operational space the SXD reaches lower density than the SND does. These facts imply that the DEMO SXD provides a larger margin in terms of lowest possible separatrix density or main plasma dilution.

(b) At $P_{\mathrm{in}} = 300$ MW, the SXD needs double the Ar concentration with respect to the SXD at $P_{\mathrm{in}} = 150$ MW at the same density. Note also that the SND curve nearly overlaps with that of the SXD at $P_{\mathrm{in}} = 300$ MW, despite a factor of 2 difference in their input power. This indicates that the SND has already largely exhausted its capability to radiate power at $P_{\mathrm{in}} = 150$ MW, while the SXD still has some margin.

(c) For a plasma within the operational space in the SXD configuration with $P_{\mathrm{in}} = 150$ MW, by raising the power input to 300 MW the plasma *may* remain inside the operational space in some cases, as indicated by the red arrows in the inset in figure 2. In contrast, we did not find an operational space for the DEMO SND at $P_{\mathrm{in}} = 300$ MW. This suggests that the SXD configuration is more robust in exhausting the power into the plasma boundary than the conventional SND on DEMO.

(d) As Ar concentration increases along the curves, the plasma density decreases in all cases, regardless of divertor configuration or power level. The curves representing different configurations or P_{in} converge at higher $n_{\mathrm{e,sep}}$. This is simply because the impurity concentration progressively becomes negligible towards higher densities, hence the effect of Ar impurities on the plasma diminishes.

We will examine item (c) and (d) in section 4 and section 5, respectively, and elaborate on (a) and (b) in the following.

The factor $\sim$2 difference in $\bar{c}_{\mathrm{Ar,sep}}$ at the same density in the SXD and SND coincides with the difference in their parallel connection length from the OMP to the outer target, which is $L_{\parallel,\mathrm{ot}}^{\mathrm{SX}}/L_{\parallel,\mathrm{ot}}^{\mathrm{SN}} \geqslant 1.75$ within a radial distance of 3 mm from the separatrix. A factor of $\sim$2 difference in $c_{\mathrm{Ar,sep}}$ is also observed when the input power in the SXD is doubled from 150 to 300 MW.

First, we introduce the model on which our analytical analysis is based; the Lengyel model [25]. It has been utilized to analyse power dissipation via impurity seeding in the plasma boundary in recent years [26–30], to estimate the impurity concentration c_z needed for dissipating the conducted power flux loss from upstream to downstream. It assumes (1) pure electron heat conduction in the parallel direction, (2) no radial transport, (3) power loss due entirely to impurity radiation, (4) homogeneous impurity concentration in the boundary layer and (5) conservation of static pressure within the impurity cooling region. With these assumptions, the c_z needed for the conduction–radiation balance is given by:

$$c_z = \frac{q_{\parallel \mathrm{u}}^2 - q_{\parallel \mathrm{t}}^2}{2\kappa_{\mathrm{e0},\parallel} n_{\mathrm{eu}}^2 T_{\mathrm{eu}}^2 \int_{T_{\mathrm{t}}}^{T_{\mathrm{u}}} L_z(T_{\mathrm{e}}) \sqrt{T_{\mathrm{e}}}\, \mathrm{d}T_{\mathrm{e}}}. \qquad (2)$$

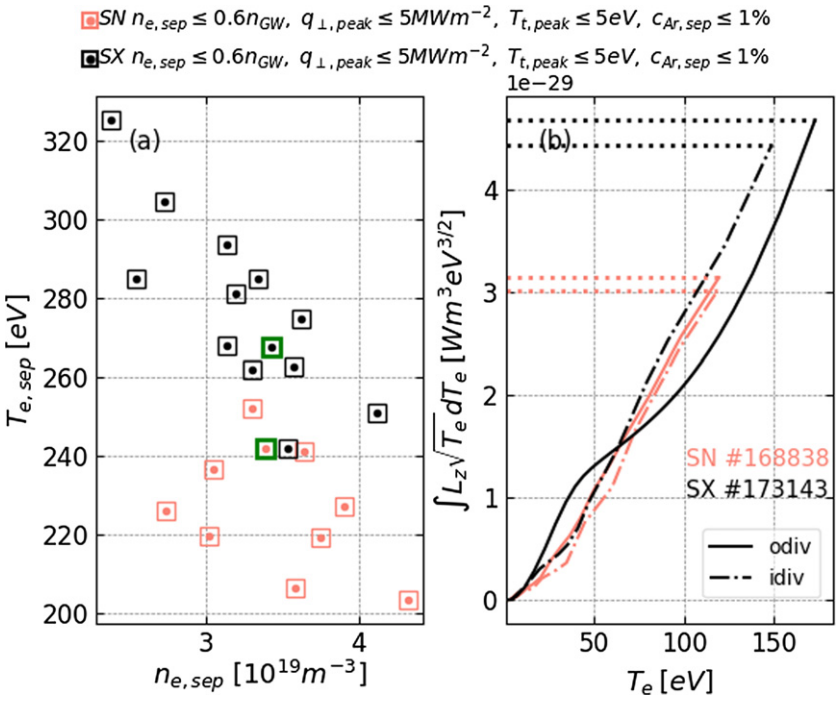

Figure 3. (*a*) Upstream separatrix temperature as a function of the upstream separatrix density for each of the simulations of the SXD and SND configurations within the operational space. (*b*) Comparison of the Lengyel integral [25] as a function of the temperature in the inner and outer divertor for the two simulations marked in a green square in (*a*) (same as the ones marked in green squares in figure 2). The two simulations have similar upstream density, as shown in figure 4.

Here, the parallel heat flux is given by $q_\parallel = -\kappa_{e0,\parallel} T_e^{5/2} \nabla_\parallel T_e$ with $\kappa_{e0,\parallel}$ being the parallel electron heat conductivity divided by $T_e^{5/2}$ and is dissipated via radiation loss; $\nabla_\parallel q_\parallel = P_{rad}$. The radiation loss is $P_{rad} = c_z n_e^2 L_z(T_e)$, with L_z being the temperature-dependent electron cooling coefficient of impurity 'z'. The integral $\int_{T_t}^{T_u} L_z(T_e)\sqrt{T_e}\,dT_e$ is henceforth referred to as the *Lengyel integral* and denoted as L_{int}. L_{int} is dependent on T_e and represents the temperature-dependent part of the power dissipation by an impurity. We can see that the parameters that dictate the value of c_z are the parallel heat flux reduction, electron temperature and upstream pressure ($n_{eu}T_{eu}$).

As investigated in [28], as well as shown in figure 3(*b*), L_{int} has nearly *linear* dependence on T_{eu} for the Ar impurity, $L_{int} \propto T_e$. Within the operational space, the power flux downstream at the target is $q_{\perp t} \leqslant 5$ MW m^{-2}. The $q_{\parallel t}^2$ at the target is negligible compared to $q_{\parallel u}^2$ at the upstream. Therefore, the c_z in equation (2) can be rewritten as:

$$c_z \propto q_{\parallel u}^2/(2\kappa_{e0,\parallel} n_{eu}^2 T_{eu}^3). \tag{3}$$

Substituting the two-point model formula of $T_{eu} \approx (\frac{7}{2}\frac{q_{\parallel u}L_\parallel}{\kappa_{e0,\parallel}})^{2/7}$ into equation (3) we obtain:

$$c_z \propto \frac{q_{\parallel u}^{8/7}}{n_{eu}^2 L_\parallel^{6/7}}. \tag{4}$$

This equation reveals that, on the one hand, at the same density and same power flux upstream, the average Ar concentration needed to dissipate all the conductive power flux from upstream is almost *inversely proportional* to the connection length from the midplane to the outer target. On the other hand, with the parallel connection length being the same (i.e. same configuration), the average Ar concentration scales nearly linearly with the upstream power flux.

Being inside the operational space requires a cold divertor plasma condition of $q_{\perp,t} \leqslant 5$ MW m^{-2} and $T_t \leqslant 5$ eV. This means that $q_{\parallel t}^2 \ll q_{\parallel u}^2$ and that the simulations within the operational space can indeed be described by equation (4). Now the observed difference in Ar concentration between the SXD and SND and between the SXD with $P_{in} = 150$ MW and $P_{in} = 300$ MW agrees with the analytical model prediction. The trends discussed in item (a) and (b) above are captured by equation (4). First, for the DEMO SND and SXD, assumed to have the same λ_q, their upstream power flux is similar at the same input power of $P_{in} = 150$ MW. The difference in Ar concentration between the two configurations is thus decided by their parallel connection length. Within the radial range of λ_q of 3 mm, their connection lengths to the outer target give $L_\parallel^{SX}/L_\parallel^{SN} \geqslant 1.75$. The Lengyel model thus predicts that the averaged Ar concentration of the SXD and SND plasma within the operational space in the plasma boundary is $\bar{c}_{Ar}^{SX} / \bar{c}_{Ar}^{SN} \approx 0.57$. This value is very close to the factor ~2 difference observed in figure 2, which explains the cause of point (a). Second, for the SXD at input power of 150 and 300 MW where the parallel connection length is the same, according the equation (4), at the same upstream density the Ar concentration in simulations within the operational space is proportional to the upstream parallel power flux, which in effect is proportional to the input

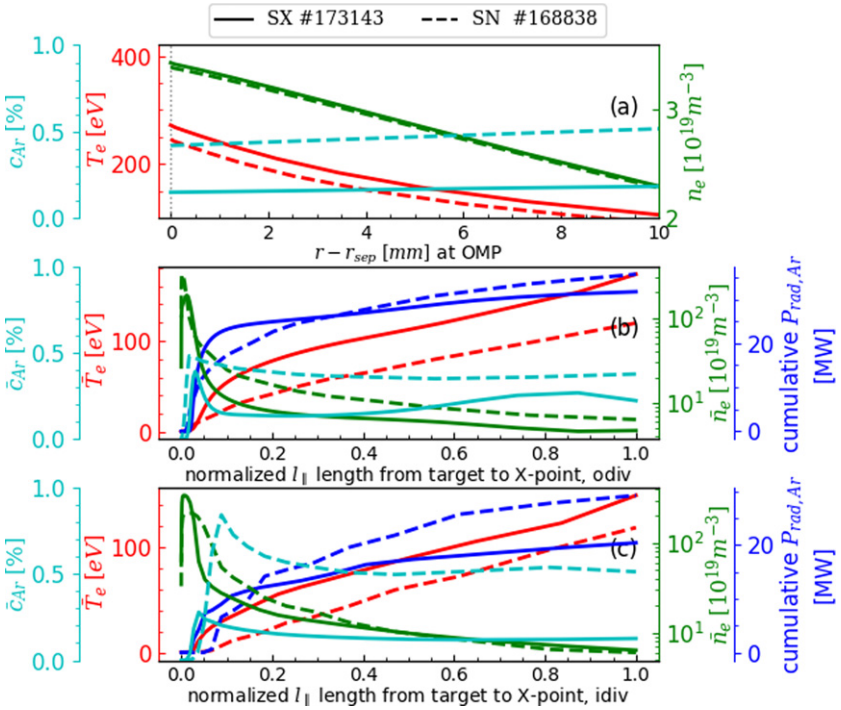

Figure 4. (*a*) Radial profiles of T_e, c_{Ar} and n_e in the near SOL at the OMP. (*b*) Parallel profiles in the outer divertor. $\bar{T}_e$ is the average electron temperature weighted by the number of particles in the cells, $\bar{n}_e$ is the cell volume weighted average of electron density and $\bar{c}_{Ar}$ is the cell volume weighted average of Ar concentration in the radial range of 3 mm mapped to the OMP. Blue curves are the cumulative sum, starting from the divertor target, of the radiated power by Ar impurity in the divertor region. (*c*) Parallel profiles of the same parameters as in (*b*) along the normalized parallel length in the inner divertor. Since the SXD and SND are very different in their outer divertors, we focus our analysis on the outer divertor. Parameters in the inner divertor are nevertheless provided as a reference.

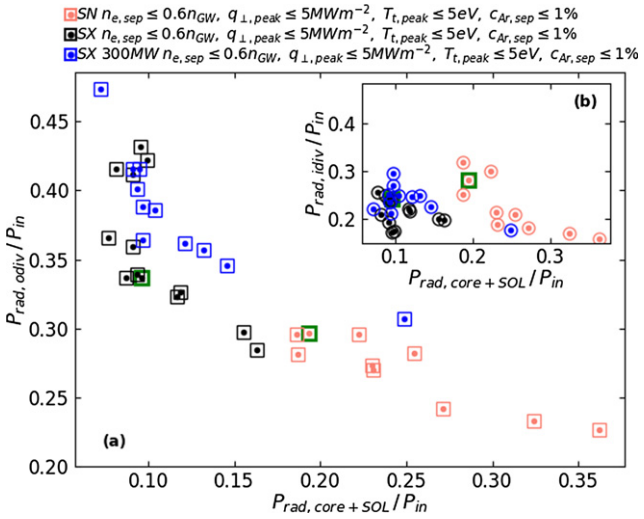

Figure 5. Radiated power in the outer divertor as a function of the fractional radiated power from the 'core' and SOL region (see definition in figure 1) above the X-point, both as a fraction of the input power P_{in}. Only the simulations within the operational space are shown here for the DEMO SXD at $P_{in} = 150$ MW and $P_{in} = 300$ MW, and the SND at $P_{in} = 150$ MW. The two simulations marked in green squares are the same ones as similarly marked in figure 2 and figure 3(a).

power. Hence, for the SXD at $P_{in} = 150$ and 300 MW, with the input power doubled, the $\bar{c}_{Ar,sep}$ of the plasma within the operational space is predicted to double as well. Therefore, what we stated above in point (b), comparing the 300 and 150 MW simulations, is also explained by equation (4).

As explained in section 2.1, longer connection length is beneficial in two ways: (1) when T_{eu} is comparable, longer connection length means lower temperature at the target; (2) when T_{et} is similar, configuration with longer connection length has higher upstream temperature. In figure 3(*a*), the electron temperature T_e at the OMP separatrix is shown as a function of the densities at the same location for the SXD and SND simulations within the operational space. The simulations within the operational space all satisfy $T_{t,peak} \leqslant 5$ eV, i.e. similar temperatures at the target. We see that indeed the SXD simulations have higher upstream temperature than the SND ones. This means that (1) the core plasma might be hotter and- (2) with a higher temperature upstream and similar temperature at the target, the divertor plasma is more *capable*[7] of power dissipation via radiation.

3.2. Comparison of the SXD and SND at the same upstream density

3.2.1. Radial and parallel profiles. Now, we demonstrate that the SXD may be more *capable* of dissipating power, particularly in the outer divertor than the SND. We select two simulations, marked with green squares in figure 3(*a*), of the SXD and SND at similar upstream density. These two simulations are also marked out in figures 2, 5 and 9 to

[7] Being more *capable* does not only mean that it radiates more away power at the same Ar concentration and plasma density. It can also mean that it could achieve the same amount of radiated power with less Ar concentration or lower density.

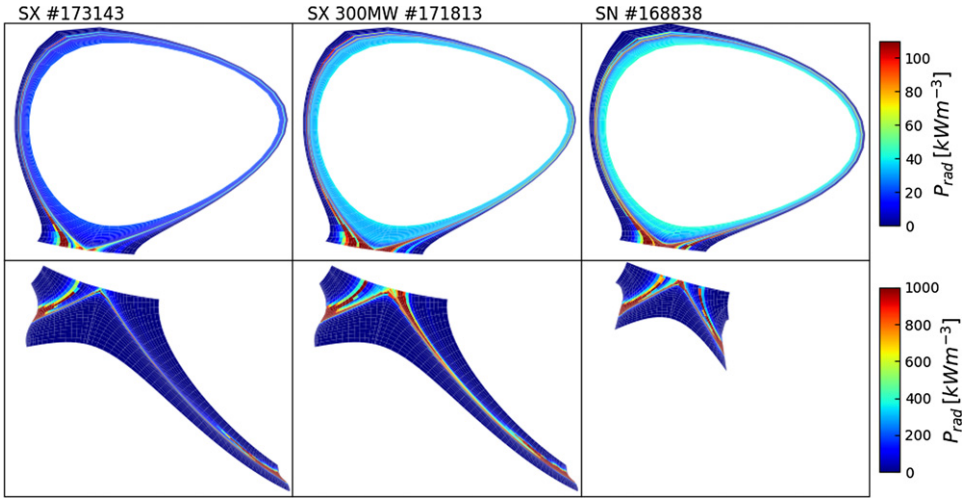

Figure 6. Total radiated power density distribution in the modelling domain for three selected simulations outlined by the grey ellipse in figure 2, which are simulations within the operational space with similar upstream density. Upper row shows the radiation density distribution in the regions above the X-point, i.e. in the 'core' and SOL. Lower row shows the radiation density distribution in the divertor region. Different configurations are shown on the same spacial scale.

show how the two simulations compare in terms of upstream Ar concentration and radiation distribution. The profiles of some relevant parameters are shown in figure 4 for the two simulations. The radial profiles in figure 4(*a*) indicate that the two simulations have the same upstream density. However, the SXD plasma maintains a higher electron temperature and lower Ar concentration in the SOL. Along the parallel direction in the *outer* divertor, the SXD still maintains a higher $\bar{T}_{\rm e}$, but a lower $\bar{n}_{\rm e}$ along most parts of the parallel length of the divertor. Here, $\bar{T}_{\rm e}$ is the radial average of electron temperature weighted by the number of particles in each cell and $\bar{n}_{\rm e}$ is the radial average of electron density weighted by the cell volume in the radial range of 3 mm mapped to the OMP. Namely, $\bar{T}_{\rm e} = \int_{\rm sep}^{\rm sep+3\ mm} T_{\rm e}(r) n_{\rm e}(r) V_{\rm cell}(r) / \int_{\rm sep}^{\rm sep+3\ mm} n_{\rm e}(r) V_{\rm cell}(r)$, and $\bar{n}_{\rm e} = \int_{\rm sep}^{\rm sep+3\ mm} n_{\rm e}(r) V_{\rm cell}(r) / \int_{\rm sep}^{\rm sep+3\ mm} V_{\rm cell}(r)$, with $V_{\rm cell}$ being the cell volume. The cumulative radiated power by Ar, starting from the divertor target, increases sharply in the first 10% of the parallel length of the outer divertor. The position of the sharp increase of the Ar radiation corresponds to the location of a large electron temperature drop. The total radiated power by Ar in the outer divertor of the SXD (30 MW) is comparable to that of the SND (35 MW), despite the Ar concentration being a factor of ∼2 lower in the SXD and the electron density also being lower. The reason for this will be demonstrated in figure 3(*b*). In the *inner* divertor, the situation is similar to that in the outer divertor, except that now the difference in $P_{\rm rad,Ar,idiv}$ is about factor ∼1.5 while $c_{\rm Ar,idiv}$ is about factor ∼3.3 lower in the SXD. In figure 3(*b*), we compare the Lengyel integral $L_{\rm int}$ in the inner and outer divertor of the two simulations as a function of $T_{\rm e}$. Note that $T_{\rm e}$ used here is the radial averaged value in the radial range of 3 mm mapped to the OMP, as explained previously. To be consistent, we also calculate the radial average of L_z, weighted by the number of particles in each cell. The $L_{\rm int}$ is calculated using the radially averaged values $\bar{T}_{\rm e}$, $\bar{L}_z$ and $\sqrt{\bar{T}_{\rm e}}$ in the inner and outer divertor. One can see from figure 3(*b*) that, due to the higher upstream temperature achieved in the SXD, $L_{\rm int}$ reaches higher values in the divertors compared to in the SND plasma. Equation (2) indicates that, to dissipate a certain amount of heat flux via radiation, having larger $L_{\rm int}$ in the plasma boundary means *less* Ar concentration will be needed, given similar upstream heat flux and electron pressure.

3.2.2. Radiation patterns. In addition to the advantage outlined in point (a), the DEMO SXD configuration has a more advantageous radiation pattern than the SND. Illustrated in figure 5 is the total radiated power in the outer divertor against the radiation above the X-point, both as a fraction of the input power. Shown here are only simulations within the operational space. We see that, consistent with the lower level of Ar impurity concentration along the separatrix, the radiation from the main plasma region ('core' + SOL) in the SXD is always lower than that in the SND at the same input power of $P_{\rm in} = 150$ MW. The radiated power fraction above the X-point is between 7%–16% in the SXD and between 19%–36% in the SND. This suggests that the DEMO SXD configuration needs *less* radiation from the main plasma region to be within operational parameter space. At the same time, the radiated power inside the *outer* divertor for the simulations within the operational space is significantly higher in the SXD than in the SND, the largest difference being around factor ∼2. However, the advantage is less marked for the inner divertor leg where the two configurations exhibit more comparable radiation capability, as shown in figure 5(*b*). The figure also illustrates that when the input power is doubled, the radiation fraction in the outer divertor, and to a lesser degree in the inner, *can* be higher at the same main plasma radiation fraction. Namely, the outer divertor leg of the SXD configuration *can* radiate even more efficiently at higher input power, keeping the radiation in the main plasma region low.

This is also confirmed in figure 6 where the 2D radiation distributions for three simulations are shown. These three simulations, outlined by the grey ellipse in figure 2, have similar upstream density. Here, we clearly see that the radiation above the main plasma region is lowest in the SXD with

$P_{in} = 150$ MW and highest in the SND at $P_{in} = 150$ MW. Note that the absolute radiated power from above the X-point in the SXD with $P_{in} = 300$ MW is still slightly lower than that in the SND with $P_{in} = 150$ MW, despite double the input power. Apart from this, figure 6 also reveals two things about the radiation pattern in the divertor region. First, the divertor radiation is largely confined close to the targets in the SXD at $P_{in} = 150$ MW, whereas in the SND it extends along the length of the divertor leg to the X-point. Second, when the input power is doubled to 300 MW in the SXD, the radiation in both the inner and outer divertor legs extends towards the X-point, now resembling the patterns in the SND. Besides the extension upwards along the poloidal direction, the strong radiation band in the outer divertor also expands in the radial direction at $P_{in} = 300$ MW, compared to the SXD at $P_{in} = 150$ MW.

4. Understanding the robustness of the SXD

As pointed out in item (c) in section 3.1, when the input power is doubled from 150 to 300 MW while the fuelling and seeding rates are kept the same in the SXD simulations, e.g. the three pairs of simulations indicated by the red arrows in figure 2, the plasma, by adjusting itself to higher density and Ar concentration levels, successfully dissipates the extra power without requiring unacceptable Ar concentration. In order to identify what changed in the plasma that ultimately enabled it to exhaust double the amount of power and stay within the operational space of the SXD configuration, we look at one of these pairs of simulations in detail.

With P_{in} increased from 150 to 300 MW at the same fuelling and seeding rate, the upstream plasma evolves to be slightly denser, as indicated in figure 2, as well as much hotter. The radial profiles at the OMP in figure 7 show that the density is only factor $\sim$1.09 higher (*by* 9%), while the temperature is factor $\sim$1.43 higher (*by* 43%) in the radial width of 3 mm (λ_q) from the separatrix. The electron static pressure in the denser and hotter plasma is hence about factor $\sim$1.5 higher. We also note that the local (OMP) Ar concentration is higher across the width of the SOL at the higher power input. Between the SXD and SND, as discussed in section 3.1, at the same upstream density (*concentration*) the SXD has *lower* concentration (*density*). This is an essential advantage of the SXD, as here we observe that the plasma shifts to higher density and higher concentration when the power input is doubled. The direct reason the DEMO SND does not have operational space at $P_{in} = 300$ MW may be that it needs too high density ($n_{e,sep} > 0.6 n_{GW}$) and/or too high Ar concentration ($c_{Ar,sep} > 1\%$) to achieve safe divertor conditions ($q_{\perp,t} \leqslant 5$ MW m^{-2} and $T_t \leqslant 5$ eV), as the density and concentration are already high at $P_{in} = 150$ MW in this configuration.

Indeed, the Ar concentration increases everywhere in the simulation domain at higher input power in the SXD, as demonstrated by figure 8(*b*). The concentrations shown here are the average value in each region weighted by the cell volume. Outside the separatrix, the average is calculated over grid cells within the width of 3 mm from the separatrix. One can see that the average Ar concentration is about $\times$1.5 higher in both the outer divertor and inner divertor. The Ar concentration increases particularly significantly in the main plasma ('core' + SOL) but the absolute values there remain low (<0.32%), and as can be seen in figure 8(*a*), the radiated power in these two regions stays low as well. The radiated power, decomposed by species (D or Ar) and by region, is shown here in figure 8(*a*). It can be seen here that the enhancement of the radiation at $P_{in} = 300$ MW is contributed predominantly by the Ar impurity, since the radiated power by D, $P_{rad,D}$, is smaller and increases less significantly. The Ar radiation in the domain increases by 150%, while in comparison D radiation increases just by about 88%. The enhancement in Ar radiation causes the total radiation to increase by 130%, more than the 100% increase in the input power P_{in}. Corresponding to the increase in averaged Ar concentration in each region, the radiation increases in all regions at higher input power. In both the 150 and 300 MW simulations, the radiation is concentrated in the divertor region. The radiation is enhanced, particularly in the divertor region, with the absolute radiated power being about a factor of $\sim$2.3 higher in the $P_{in} = 300$ MW simulation in both the inner and outer divertor legs. Because of the more than doubled enhancement of impurity radiation in the divertor region in the SXD configuration, the plasma is able to stay within the operational space when the input power is increased from 150 to 300 MW.

To understand *why* Ar radiation can greatly increase in the divertor region in the higher power plasma, we return to the Lengyel model expressed by equation (2). Given that for plasma within the operational space $q_{\parallel,t} \ll q_{\parallel,u}$, we reform the equation as:

$$q_{\parallel u} \approx \sqrt{2\kappa_{e0,\parallel} c_z (n_{eu} T_{eu})^2 L_{int}}. \quad (5)$$

Multiplying by the contact surface area, the rhs yields the total power loss due to impurity radiation (Lengyel model assumption (3)) in the region between the upstream and the target. The three terms that regulate the radiated power in this equation are: c_z, $n_{eu}T_{eu}$ and the *Lengyel integral*, L_{int}. As pointed out above, due mainly to the increase in upstream temperature T_{eu} at $P_{in} = 300$ MW the electron static pressure $p_{eu} = n_{eu}T_{eu}$ is about factor $\sim$1.5 higher. In addition, the average Ar concentration within the distance of λ_q of 3 mm from the separatrix in the divertor region $\bar{c}_{Ar,odiv}$ and $\bar{c}_{Ar,idiv}$ is factor $\sim$1.5 higher at $P_{in} = 300$ MW, compared to the SXD plasma at $P_{in} = 150$ MW. The remaining term is L_{int}, which depends on the electron temperature T_e. Because the electron cooling coefficient L_z drops by several orders at temperatures below 5 eV, the integration is not sensitive to the exact value of T_t as long as it is $\leqslant$5 eV. Therefore, for simulations within the operational space, the L_{int} depends only on T_u. The electron temperature increases from the target to upstream along each single flux tube. We calculate the average L_{int} within 3 mm radial distance from the separatrix mapped to the midplane in the inner and outer divertor in the same way as explained in section 3.1. We display the calculated L_{int} as a function of the temperature in figure 8(*c*). The position of the upper limit of the temperature for the integration is marked in figure 8(*d*), which also shows the Ar electron cooling function from ADAS

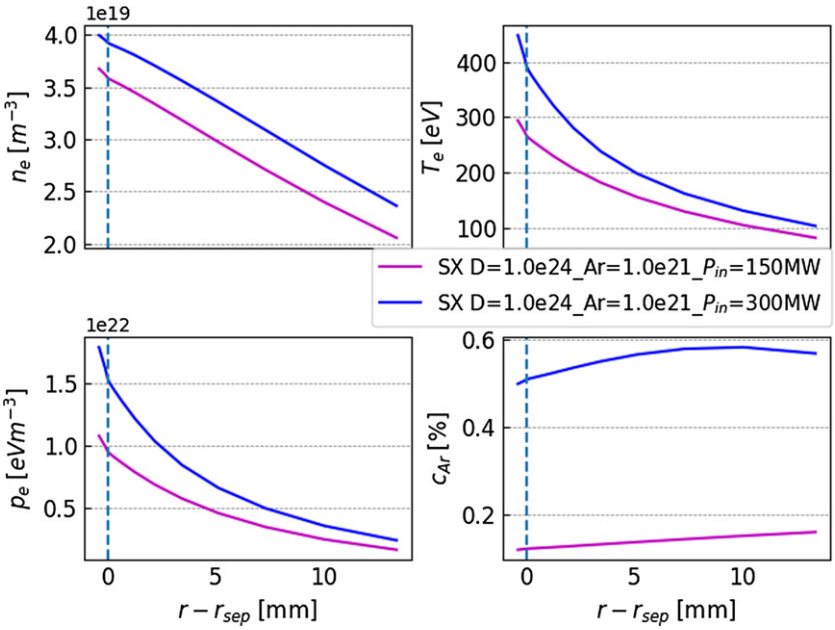

Figure 7. Radial profiles of electron density, temperature, static pressure and Ar concentration at the OMP in two DEMO SXD simulations with the same D fuelling and Ar seeding rates at $P_{\rm in} = 150$ MW and $P_{\rm in} = 300$ MW. The two simulations shown here are the two simulations marked by the right-most red arrow with blue outline in figure 2.

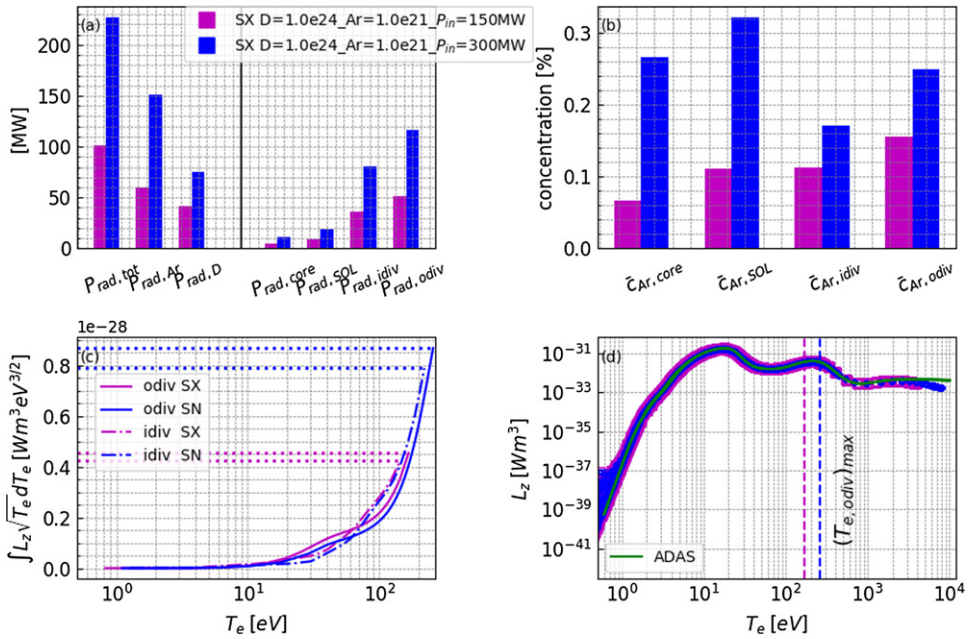

Figure 8. Comparison of various parameters of the plasma for two DEMO SXD simulations with the same D fuelling and Ar seeding rates at $P_{\rm in} = 150$ MW and $P_{\rm in} = 300$ MW, marked by the right-most red arrow with blue outline in figure 2. (*a*) Radiated power fractions, $f_{\rm rad,\#}$ with respect to $P_{\rm in}$, with #' denoting radiation of a species from the entire modelling domain or radiation in a region from all the species. (*b*) Averaged Ar concentration in each region. (*c*) Average *Lengyel integral* (defined in section 3.1) as a function of $T_{\rm e}$ in the flux tubes within a distance of λ_q of 3 mm from the separatrix in the inner and outer divertor. (*d*) Electron cooling coefficient calculated from the modelling results and from the ADAS database. Vertical dashed lines mark the radial average of the temperature at the divertor entrance at the poloidal location of the X-point, which is also the upper bound of the temperature over which the Lengyel integral is calculated.

and that obtained from the simulation. In this figure, it can again be seen that $L_{\rm int}$ increases nearly linearly with the upper bound of the temperature forAr impurity. Because the temperature at the divertor entrance is higher in the $P_{\rm in} = 300$ MW case, the $L_{\rm int}$ in the inner and outer divertor leg reach larger values. The integral is factor ∼1.9 higher in the outer divertor and inner divertor, compared to the standard $P_{\rm in} = 150$ MW case. Inserting the factors of differences in $n_{\rm eu}T_{\rm eu}$, c_z and the $L_{\rm int}$ into the rhs of equation (5), we have that $\left(\sqrt{c_z(n_{\rm eu}T_{\rm eu})^2L_{\rm int}}\right)_{300\ \rm MW} / \left(\sqrt{c_z(n_{\rm eu}T_{\rm eu})^2L_{\rm int}}\right)_{150\ \rm MW} \approx$ 2.5, in both the outer and inner divertor. This is close to the

observed factor ∼2.3 higher of Ar radiation in the divertors and 150% increase in domain. Therefore, the combined result of elevated upstream electron pressure, Ar concentration and larger values of *Lengyel integral* enables the plasma to exhaust the extra power in the divertor region, when the input power is doubled in the SXD configuration and the fuelling and seeding rates remain the same. We point out that the increases in electron pressure and Lengyel integral are *both* due to an increase in the upstream electron temperature. This is plain to see when we examine two SXD simulations at similar upstream density with $P_{\rm in} = 150$ MW and $P_{\rm in} = 300$ MW, both within the operational space. The Ar radiation in the outer divertor of these two is different by about a factor of ∼2.4. The temperature alone being factor ∼1.6 higher in the 300 MW case, causing the electron pressure andLengyel integral to be factor ∼1.6 and factor ∼1.8 higher, respectively. Combined with the change in the Ar concentration level, we reproduce with equation (5) the factor of change of Ar radiation in the divertors.

5. Impurity seeding affecting upstream plasma density

Finally, we look into point (d) raised in section 3.1. Here, we will explain the observed plasma density drop with increasing Ar concentration. As this is observed for different configurations and input powers examined in this work, we focus on the DEMO SXD at standard $P_{\rm in} = 150$ MW.

A similar reduction in the main plasma density is observed in ITER simulations with neon seeding with a more complete model using kinetic neutrals and unbundled neonbeing used [31, 32]. In [32], the simulations have been grouped into different radiation levels and $c_{\rm Ne,sep}$ is found to be $\propto n_{\rm e,sep}^{-2}$ at low radiated power, i.e. low $c_{\rm Ne,sep}$, and $\propto n_{\rm e,sep}^{-4}$ at high radiated power. One can see in figure 2 that the DEMO modelling results of simulations within the operational space, which have high impurity radiation, agree with the $c_{z,\rm sep} \propto n_{\rm e,sep}^{-4}$ scaling in ITER. As pointed out in [32], unfortunately there has been little attention paid to this in the experiments so far.

Next, we try to explain the drop in main plasma density with Ar seeding in the simulations. The radiated power by Ar is directly correlated with the increase in concentration of this impurity, as shown in figure 9. With Ar impurity radiating away more power from the plasma, from a power balance point of view, the power available for ionizing D neutrals, coming from gas puff or neutralization at PFC surfaces, is reduced. We define the parameter $P_{\rm recycle} = P_{\rm in} - P_{\rm rad,Ar} - P_{\rm load,mcw} - P_{\rm load,pfr} - P_{\rm load,tar}$ as a measure of the power available for ionizing D neutrals. Here, $P_{\rm load,mcw}$, $P_{\rm load,pfr}$ and $P_{\rm load,tar}$ are the power deposited onto the mcw, the PFCs below the private flux region (pfr), and the divertor targets. The $P_{\rm load,mcw}$ and $P_{\rm load,pfr}$ terms, which resulted from radial transport, are relatively constant and small throughout the fuelling and seeding scan in the SXD with $P_{\rm in} = 150$ MW, standing at about ⩽20% of the input power. The power load to the outer and inner targets $P_{\rm load,tar}$ is also usually comparably small, especially for the simulations within the operational space. Note that $P_{\rm recycle}$ is not equivalent to $P_{\rm rad,D}$. While the latter is simply the power radiated by D,

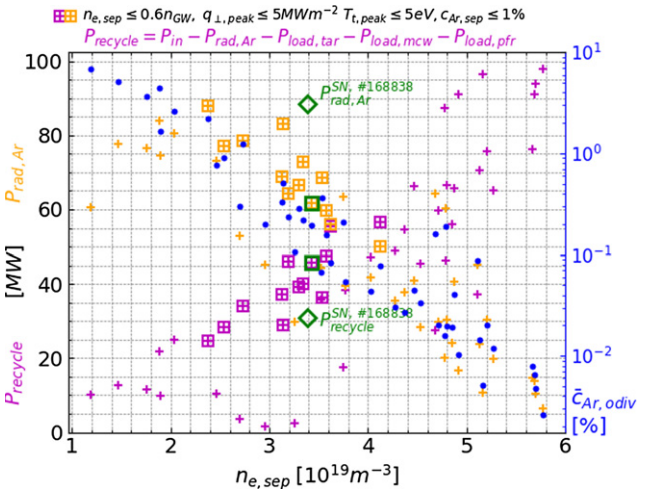

Figure 9. Radiated power by Ar in the plasma, $P_{\rm rad,Ar}$ (*orange*), the power available for ionizing D neutrals, $P_{\rm recycle}$ (*magenta*), and the average Ar concentration in the divertor region within the radial range of λ_q of 3 mm (*blue*), as a function of the OMP separatrix density, for the DEMO SXD at $P_{\rm in} = 150$ MW. Simulations within the operational space are marked with square symbols. The SXD simulation chosen for comparison in figure 3(*b*) is marked with green squares. The values of $P_{\rm rad,Ar}$ and $P_{\rm recycle}$ of the SND simulation to which the SXD simulation was compared in figure 3(*b*) are also given and marked in hollow green diamond symbols here.

the former includes the latter as well as the power that becomes the potential energy of the D ions during an ionization event. Figure 9 clearly reveals that there is evidently an *anti-correlation* between $P_{\rm rad,Ar}$ and $P_{\rm recycle}$ at fixed power input, when the other terms in the expression for $P_{\rm recycle}$ are small compared to $P_{\rm rad,Ar}$. As the former increases with the rising Ar concentration, the amount of power that goes into ionizing D neutrals, $P_{\rm recycle}$, drops from close to 100 MW at the highest to just about 20 MW at the lowest. There are several data points whose $P_{\rm recycle}$ at intermediate density of 2–4 $\times 10^{19}$ m^{-3} deviates from the quasi-linear trend. These are simulations outside the operational space and with large total power load to the targets ($P_{\rm load,tar} \approx$ 60–100 MW), due to *insufficient* high upstream density or Ar radiation. Indeed, for the simulations within the operational space with $T_{\rm t} \leqslant 5$ eV, where the assumption that the $P_{\rm load,mcw}$, $P_{\rm load,pfr}$ and $P_{\rm load,tar}$ terms are small compared to $P_{\rm rad,Ar}$ is valid, the anti-correlation between $P_{\rm rad,Ar}$ and $P_{\rm recycle}$ is much clearer.

Ignoring the radiative loss during recombination of D^+, we have $P_{\rm recycle} = S_n^{\rm D^+} \times (\epsilon_H^{\rm pot} + \epsilon_H^{\rm rad})$, with $\epsilon_H^{\rm pot} = 13.6$ eV (no molecules in the simulation), $\epsilon_H^{\rm rad}$ being the mean D radiation loss per ionization event and $S_n^{\rm D^+}$ being the particle source in p s^{-1}. As $S_n^{\rm D^+}$ concentrates in a narrow region of $T_{\rm e} = 5$–10 eV in the dense divertor plasma, $\epsilon_H^{\rm rad}$ does not vary much [33], yielding a linear dependence of $S_n^{\rm D^+}$ on $P_{\rm recycle}$. This linear dependence between the two parameters is demonstrated in figure 10(*a*), for simulations of the DEMO SXD configuration at lower (50 MW), standard (150 MW) and higher (300 MW) input power. The magnitude of the input power limits the range over which the power available for ionizing D atoms can change. This then determines the range over which the ionization particle source can change in the simulations.

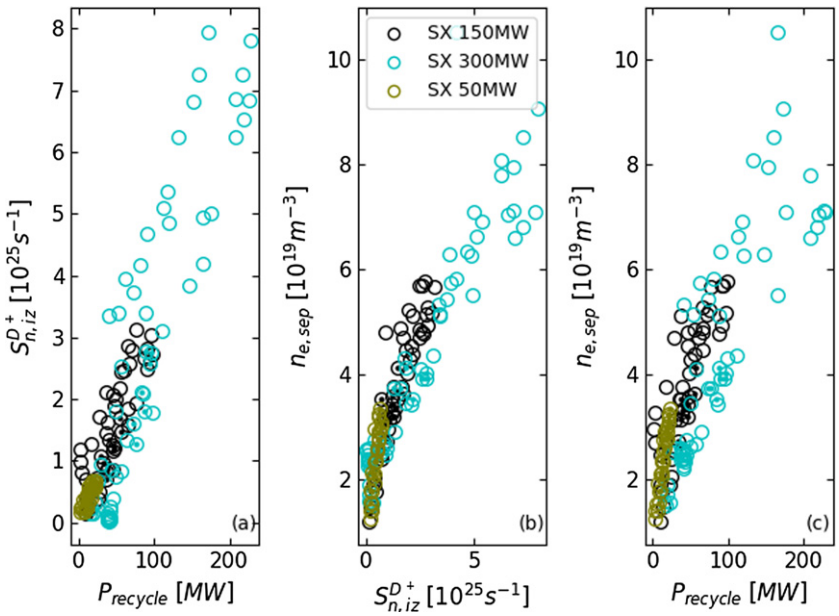

Figure 10. Correlation between P_{recycle} and $S_n^{\mathrm{D}^+}$, $S_n^{\mathrm{D}^+}$ and n_{e}, P_{recycle} and n_{e} for the SXD simulations with low (50 MW), standard (150 MW) and high (300 MW) power input. P_{recycle} is the power available for ionizing the D neutrals. $S_n^{\mathrm{D}^+}$ is the ionization particle source of D^+. n_{e} is the density at the OMP separatrix.

The ionization particle source has a direct impact on the plasma density, as shown in figure 10(*b*). With a more abundant ionization particle source in the plasma, the plasma density increases. Finally, via the effect on the ionization particle source, P_{recycle} can affect the plasma density, as demonstrated in figure 10(*c*). The plasma density is positively correlated with the power that goes into ionizing the D neutrals. Therefore, the observation of plasma density dropping with increasing Ar concentration at each input power level is explained as the following: higher amount of Ar in the plasma enhances the radiated power, which causes the power available for ionizing D neutrals to decrease. This results in fewer ionization events of D neutrals and consequently less particle (ions and electrons) source in the plasma. With less particle source available, the plasma density subsequently drops. The picture described here echoes the discussion in section 3.2.3 in [32].

6. Summary and discussion

In this work, we have reported the following three key results found in the exploration of operational space in DEMO with super-X and conventional SNDs via fuelling, seeding and power level scans.

We find that the SXD configuration offers a larger margin to the limits on plasma density and impurity concentration of the operational space. Namely, at the same upstream density (Ar *concentration*) the DEMO SXD has lower Ar concentration (*upstream density*) at the vicinity of the confined plasma compared to the DEMO SND. Utilizing the simple Lengyel model, we establishthe fundamental reason for the larger margin in the SXD to be the longer parallel connection length from upstream to the outer target in this configuration. Furthermore, the SXD configuration features less radiation from above the X-point and higher radiation from within the outer divertor, with respect to the SND configuration. In the divertor, the radiation is mainly confined close to the target in the SXD at input power of 150 MW. In contrast, in the SXD with double the power (300 MW) and in the SND (150 MW), the radiation in the divertor extends poloidally upwards to the X-point and spreads radially outwards.

At input power of 300 MW, DEMO with the SXD still attains operational plasma states, whilst DEMO with the conventional SND does not. Comparing the 300 MW simulation to the standard 150 MW one at the same fuelling and seeding rates in the SXD configuration, both within the operational space, we find that the radiated power by Ar impurity more than doubled, a more significant increase than that of the input power. The enhancement of the radiation is due to the elevated Ar concentration in the divertor as well as the elevated upstream plasma density (by about 10%) and temperature (by about 40%), which results in higher electron pressure upstream and larger Lengyel integral in the divertor in the 300 MW simulations. This scheme can be well explained by the Lengyel model.

Finally, we observe that the plasma density drops with increasing Ar concentration in DEMO in all configurations (SXD or conventional SND) and at all input power levels (50, 150, 300 MW). The most important reason for this is that Ar impurity radiates away more power as the impurity concentration increases, leaving ever less power available for D atoms to be ionized.

We point out that the choice of $\lambda_q = 3$ mm might be optimistic. Given a smaller λ_q, e.g. 1 mm, the amount of heat flux that needs to be removed is even tripled, requiring the plasma to be further cooled before it arrives at the divertor

targets. In this case, it might be possible for us to achieve a DEMO plasma with both acceptable divertor condition and impurity level in the vinicity of the main plasma. However, the advantage of the SXD over SND that we have discussed so far still holds. Even though simulations for current machines with kinetic neutrals, including molecules, the neutral-wall and neutral-neutral interactions, resulted in different neutral distributions and divertor plasma conditions than the simulations with fluid neutrals [20]. As already mentioned in section 1, the DEMO boundary plasma is dense enough that the neutrals' mean free path in the divertor is much smaller compared to the size of the divertor, justifying to some extent the treatment of neutrals as fluids in the simulations in this work. Nevertheless, the puffing and pumping in the fluid neutrals model are treated in simplistic ways, posing concerns with regard to the obtained results. However, we did pumping coefficient scan and found that the plasma density is not sensitive to the scan in steady state. The c_z as a function of n_e based on the Lengyel model is valid for plasma conditions at and after divertor detachment onset. In this work, we instead see that the simulations with one target in attached condition (the *dots* with $n_{e,sep} \leqslant 4.4 \times 10^{19}$ m^{-3} in figure 2) also fit into the $\bar{c}_{Ar,sep} - n_{e,sep}$ curve in figure 2. Further analysis is needed to understand why those simulations fit the curve. Another detail is that the c_z in the Lengyel model is the constant impurity concentration in the divertor region. In this work, we have chosen to focus on $\bar{c}_{Ar,sep}$ as a measure of the impurity level in the immediate vicinity of the confined plasma out of interest in core dilution. We found that the Ar concentration in the outer divertor varies linearly with the Ar concentration along the separatrix, with the Ar enrichment, which is the ratio of Ar concentration in the divertor over that upstream, scattering only slightly between 1.0–3.0 in the simulations. Therefore, $\bar{c}_{Ar,sep}$ can be easily translated into $\bar{c}_{Ar,div}$. The activation of drifts, which is not done in the simulations in this study, may modify the obtained divertor enrichment of Ar as well as alter the in/out divertor asymmetry. We observe that the in/out divertor asymmetry is different between the DEMO SXD and DEMO SND. In the DEMO SND the outer divertor is always the hot one throughout the scans whereas the DEMO SXD has a more complicated picture. Either the inner or outer divertor can be the hotter one, corresponding to the direction of a parallel thermoelectric current within the radial range of 3 mm (λ_q). We will report these interesting results in another work in the near future.

Due to the use of fluid neutrals, bundled Ar charge states and the lack of drift effects in this study, the results reported here should be noted with some caution. On the other hand, however, the simulations in this study have been carried out in a highly consistent way. We have set up simulations for all the configurations in identical ways and using the same code. Therefore, the comparative results reported here, e.g. the advantages observed in the SXD configuration for DEMO with respect to the DEMO SND, should nevertheless be noted. It will be very exciting to repeat this kind of study on other DEMO-scale future machines as in [34].

Acknowledgments

This work has been carried out within the framework of the EUROfusion Consortium and has received funding from the Euratom research and training programme 2014–2018 and 2019–2020 under Grant agreement No. 633053. The views and opinions expressed herein do not necessarily reflect those of the European Commission. This work was supported in part by the Swiss National Science Foundation.

ORCID iDs

L. Xiang https://orcid.org/0000-0001-8175-6640
F. Militello https://orcid.org/0000-0002-8034-4756
F. Subba https://orcid.org/0000-0002-8170-4792
D. Coster https://orcid.org/0000-0002-2470-9706
M. Wensing https://orcid.org/0000-0003-4462-7860
M. Wischmeier https://orcid.org/0000-0002-3065-027X
H. Reimerdes https://orcid.org/0000-0002-9726-1519

References

[1] Federici G., Giruzzi G., Lowry C., Kemp R., Ward D., Wenninger R. and Zohm H. 2013 EU DEMO design and R & D studies *2013 IEEE 25th Symposium on Fusion Engineering (SOFE)* (San Francisco, CA, USA, 10-14 June 2013) pp 1–8 (https://ieeexplore.ieee.org/xpl/conhome/6624144/proceeding)
[2] Biel W. *et al* 2019 Diagnostics for plasma control - from ITER to DEMO *Fusion Eng. Des.* **146** 465–72
[3] Federici G. *et al* 2019 Overview of the DEMO staged design approach in Europe *Nucl. Fusion* **59** 066013
[4] Lux H., Kemp R., Ward D.J. and Sertoli M. 2015 Impurity radiation in DEMO systems modelling *Fusion Eng. Des.* **101** 42–51
[5] Reimerdes H. *et al* 2020 Assessment of alternative divertor configurations as an exhaust solution for DEMO *Nucl. Fusion* **60** 066030
[6] Hirai T. *et al* 2015 Status of technology R & D for the ITER tungsten divertor monoblock *J. Nucl. Mater.* **463** 1248–51
[7] You J.H. *et al* 2016 European demo divertor target: operational requirements and material-design interface *Nucl. Mater. Energy* **9** 171–6
[8] Siccinio M., Federici G., Kembleton R., Lux H., Maviglia F. and Morris J. 2019 Figure of merit for divertor protection in the preliminary design of the EU-DEMO reactor *Nucl. Fusion* **59** 106026
[9] Aho-Mantila L. *et al* 2021 Scoping the characteristics and benefits of a connected double-null configuration for power exhaust in EU-DEMO *Nucl. Mater. Energy* **26** 100886
[10] Militello F. *et al* 2021 Preliminary analysis of alternative divertors for DEMO *Nucl. Mater. Energy* **26** 100908
[11] Stangeby P. 2000 *The Plasma Boundary of Magnetic Fusion Devices* (Bristol: IOP Publishing)
[12] Petrie T.W. *et al* 2013 Effect of changes in separatrix magnetic geometry on divertor behaviour in DIII-d *Nucl. Fusion* **53** 113024
[13] Bonnin X., Dekeyser W., Pitts R., Coster D., Voskoboynikov S. and Wiesen S. 2016 Presentation of the new SOLPS-ITER code package for tokamak plasma edge modelling *Plasma Fusion Res.* **11** 1403102
[14] Wiesen S. *et al* 2015 The new SOLPS-ITER code package *J. Nucl. Mater.* **463** 480–4

[15] Rozhansky V., Kaveeva E., Molchanov P., Veselova I., Voskoboynikov S., Coster D., Counsell G., Kirk A. and Lisgo S. 2009 New B2SOLPS5.2 transport code for h-mode regimes in tokamaks *Nucl. Fusion* **49** 025007
[16] Reiter D., Wiesen S. and Born M. 2002 Towards radiation transport modelling in divertors with the EIRENE code *Plasma Phys. Controlled Fusion* **44** 1723
[17] Reiter D., Baelmans M. and Börner P. 2005 The EIRENE and B2-EIRENE codes *Fusion Sci. Technol.* **47** 172–86
[18] O'Mullane Martin 2010 *Heavy species in ADAS* (https://phys.strath.ac.uk/adas/courses/iter_2010/iter10_heavy_species.pdf)
[19] Coster D.P., Bonnin X., Reiter D., Kukushkin A., Gori S., Krstic P., Strand P. and Eriksson L. 2009 Simulations of the edge plasma: the role of atomic, molecular and surface physics *AIP Conf. Proc.* **1125** 113–22
[20] Bonnin X. and Coster D. 2011 Full-tungsten plasma edge simulations with SOLPS *J. Nucl. Mater.* **415** S488–91 Proc. of the 19th Int. Conf. on Plasma-Surface Interactions in Controlled Fusion
[21] Bernert M. *et al* 2017 Power exhaust by SOL and pedestal radiation at ASDEX Upgrade and JET *Nucl. Mater. Energy* **12** 111–8 Proc. of the 22nd Int. Conf. on Plasma Surface Interactions 2016, 22nd PSI
[22] Huber A. *et al* 2014 Impact of strong impurity seeding on the radiation losses in JET with ITER-like wall *41st EPS Conf. on Plasma Physics* (Berlin, Germany, 23 - 27 June 2014) (http://ocs.ciemat.es/EPS2014PAP/pdf/P1.031.pdf)
[23] Loarte A. *et al* 2011 High confinement/high radiated power H-mode experiments in Alcator C-Mod and consequences for International Thermonuclear Experimental Reactor (ITER) QDT = 10 operation *Phys. Plasmas* **18** 056105
[24] Eldon D. *et al* 2019 Advances in radiated power control at DIII-D *Nucl. Mater. Energy* **18** 285–90
[25] Lengyel L. 1981 Analysis of radiating plasma boundary layers *IPP 1/191* (Max-Planck-Institut für Plasmaphysik)
[26] Kallenbach A. *et al* 2013 Impurity seeding for tokamak power exhaust: from present devices via ITER to DEMO *Plasma Phys. Controlled Fusion* **55** 124041
[27] Wischmeier M., Fable E., Lackner K., Scarabosio A., Wenninger R.P. and Zohm H. 2016 A 0D stationary model for the evaluation of the degree of detachment on the divertor plates *Plasma Phys. Controlled Fusion* **58** 125011
[28] Reinke M.L. 2017 Heat flux mitigation by impurity seeding in high-field tokamaks *Nucl. Fusion* **57** 034004
[29] Goldston R.J., Reinke M.L. and Schwartz J.A. 2017 A new scaling for divertor detachment *Plasma Phys. Controlled Fusion* **59** 055015
[30] Moulton D., Stangeby P.C., Bonnin X. and Pitts R.A. 2021 Comparison between SOLPS-4.3 and the Lengyel model for ITER baseline neon-seeded plasmas *Nucl. Fusion* **61** 046029
[31] Pacher H.D., Kukushkin A.S., Pacher G.W., Kotov V., Pitts R.A. and Reiter D. 2015 Impurity seeding in ITER DT plasmas in a carbon-free environment *J. Nucl. Mater.* **463** 591–5 PLASMA-SURFACE INTERACTIONS 21
[32] Pitts R.A. *et al* 2019 Physics basis for the first ITER tungsten divertor *Nucl. Mater. Energy* **20** 100696
[33] Stangeby P.C. 2018 Basic physical processes and reduced models for plasma detachment *Plasma Phys. Controlled Fusion* **60** 044022
[34] Tobita K. *et al* (The Joint Special Design Team for Fusion DEMO) 2019 Japan's efforts to develop the concept of JA DEMO during the past decade *Fusion Sci. Technol.* **75** 372–83